Journal of Theoretical Biology 364 (2015) 220–230

Contents lists available at ScienceDirect

Journal of Theoretical Biology

journal homepage: www.elsevier.com/locate/yjtbi

The morpho-mechanical basis of ammonite form

D.E. Moulton [a,*], A. Goriely [a], R. Chirat [b]

[a] Mathematical Institute, University of Oxford, Oxford, UK
[b] UMR CNRS 5276, Université Lyon 1, France

HIGHLIGHTS

- We develop a mechanical model for the formation of ribs in ammonite shells.
- The model is based on fundamental physical principles of the shell growth process.
- All major characteristics of ammonite form and evolutionary trends are captured.
- This work presents the first quantitative model of shell ribbing pattern.
- Enables new understanding of ammonites evolution in evo devo perspective.

GRAPHICAL ABSTRACT

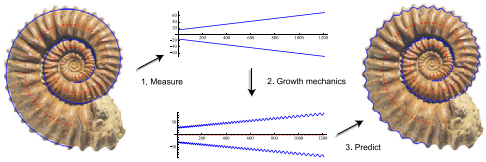

ARTICLE INFO

Article history:
Received 12 June 2014
Received in revised form
12 September 2014
Accepted 15 September 2014
Available online 26 September 2014

Keywords:
Morphogenesis
Evolution
Growth
Mathematical model
Mollusk

ABSTRACT

Ammonites are a group of extinct cephalopods that garner tremendous interest over a range of scientific fields and have been a paradigm for biochronology, palaeobiology, and evolutionary theories. Their defining feature is the spiral geometry and ribbing pattern through which palaeontologists infer phylogenetic relationships and evolutionary trends. Here, we develop a morpho-mechanical model for ammonite morphogenesis. While a wealth of observations have been compiled on ammonite form, and several functional interpretations may be found, this study presents the first quantitative model to explain rib formation. Our approach, based on fundamental principles of growth and mechanics, gives a natural explanation for the morphogenesis and diversity of ribs, uncovers intrinsic laws linking ribbing and shell geometry, and provides new opportunities to interpret ammonites' and other mollusks' evolution.

1. Introduction

Ammonites are an iconic group of extinct cephalopods. Characterised by a nearly perfect logarithmic spiral shell with regular ribbing pattern, the mathematical beauty of their form has made them a centrepiece of artistic wonder while their abundance, diversity, and high evolution rate make them a paradigm for biochronology, palaeobiology, and evolutionary theories (Gould, 2002; Eldredge, 1996; Brayard et al., 2009). The two fundamental morphological descriptors of ammonite shells are their coiling and the ribbing pattern known as commarginal ornamentation. This pattern is almost universally present in ammonites and forms along the direction of the accreted shell, appearing as an oscillation in the expansion of the shell cross-section (Fig. 1(a)). However, few authors have considered shell morphogenesis, and no previously proposed models for ammonite ribs (Checa, 1994; Hammer, 2000; Meinhardt, 2009) have produced quantitative and verifiable predictions. The starting point of our study is the notion that mechanical forces generated during growth drive tissue-scale morphogenesis and thus shape developing organisms (Hutson and Ma, 2008; Chirat et al., 2013).

* Corresponding author.
E-mail addresses: moulton@maths.ox.ac.uk (D.E. Moulton), goriely@maths.ox.ac.uk (A. Goriely), regis.chirat@univ-lyon1.fr (R. Chirat).

http://dx.doi.org/10.1016/j.jtbi.2014.09.021
0022-5193/

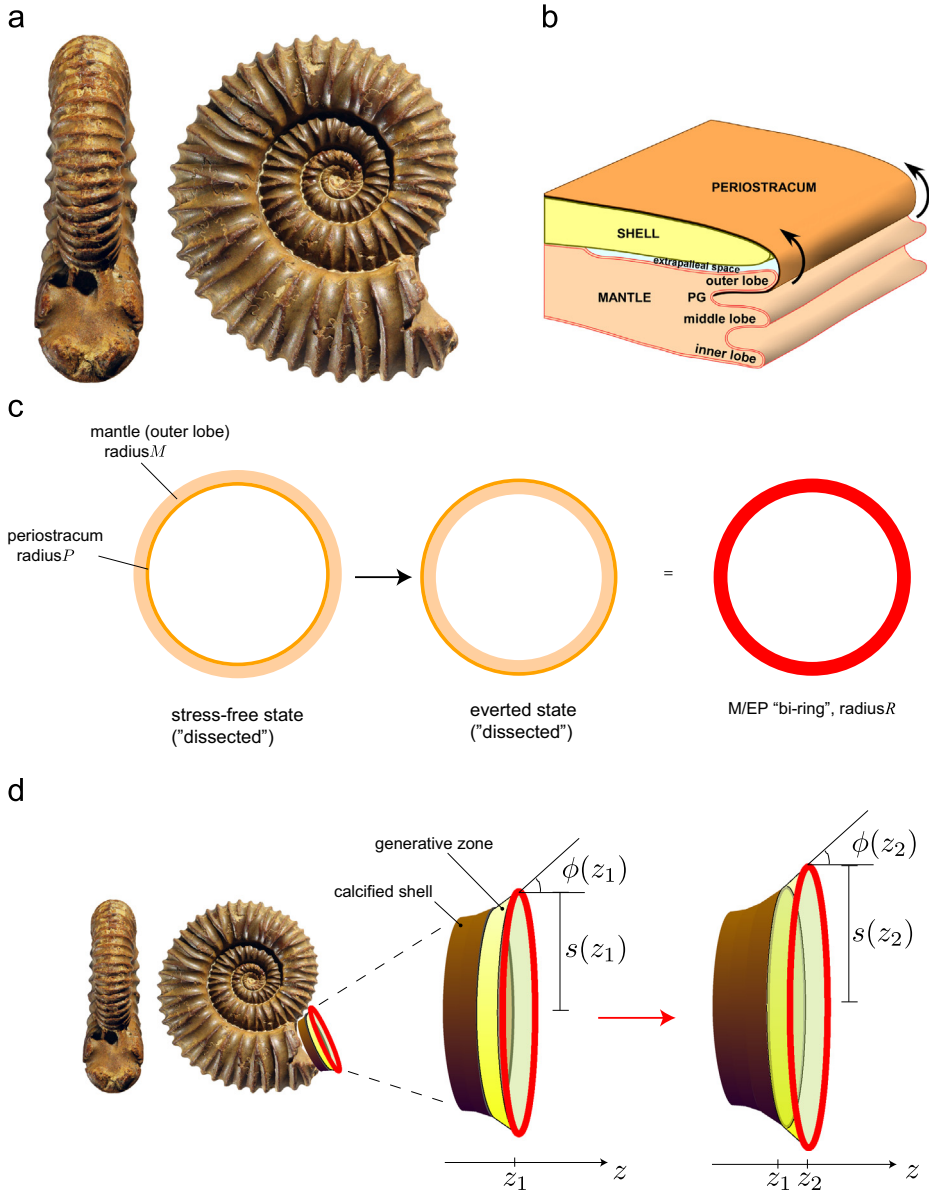

Fig. 1. Ammonite ribs and model setup. (a) Commarginal ribs in *Peltoceras schroederi*. (b) Schematic of mantle/periostracum anatomy and eversion of periostracum (PG: periostracal groove). (c) The mantle and everted periostracum (M/EP) act mechanically as a single elastic bi-ring with radius $R(z)$ when dissected from the shell. (d) Primary variables for model. The shell has radius s and orientation angle ϕ with respect to the growth axis z.

By focussing on the mechanical structure of the shell secreting system, we propose a model for ammonite morphogenesis that captures all basic features of morphological diversity and phenomenological laws observed in ammonite shell form and uncovers an intrinsic link between the shell expansion and the ribbing pattern. Many authors have argued about the functions of this ornamentation, as related to buoyancy control, camouflage, hydrodynamic efficiency, or strengthening the shell against predators (Chamberlain and Westermann, 1976; Ward, 1981; Westermann, 1996; Cowen et al., 1973; Vermeij, 1993). While these functionalist interpretations have been central within evolutionary theories, our theory provides the first predictive and *quantitative* mechanistic explanation of their form and presents new opportunities for interpreting the evolution of their shell in an evolutionary developmental biology perspective.

All modern mollusk shells are composed of an outer organic layer, called periostracum, and underlying calcified layers, all being secreted by the mantle, a thin elastic membrane lining the inner shell surface (Simkiss and Wilbur, 1989) (Fig. 1(b)). During growth, the mantle moves forward slightly beyond the calcified shell edge while secreting the periostracum, which isolates the extrapallial fluid from which the calcified shell is precipitated (Saleuddin and Petit, 1983). The periostracum is secreted in the periostracal groove, between the outer and middle mantle lobes, and is extruded between the two mantle lobes, where a stiffening process of sclerotisation takes place (Waite, 1983). It is subsequently turned inside out around the outer mantle lobe, and reaches its external position where no further thickening occurs. When calcification occurs, the periostracum becomes fixed on the outer shell surface. The unfixed periostracum surrounds the outer mantle lobe and is attached at both extremities along the calcified shell edge and inside the periostracal groove. The shape of the generative zone, namely the stiff periostracum surrounding the softer outer mantle lobe, is therefore incrementally recorded and fixed in the calcified shell during growth. In turn, the calcified shell edge acts as a template for the new growth increment. This basic structure of the mantle edge–periostracum complex has been also described in *Nautilus* (Westermann et al., 2005) and it is

reasonable to assume that the generative zone in ammonites functioned along the same principles. The puzzle of commarginal ribs is to understand how mechanical forces in the thin generative zone (of the order of a millimeter) could generate regular oscillations themselves parallel to the shell edge and of a typical scale up to 50 times larger.

2. Morpho-mechanical model

The fundamental question we ask is whether the morphogenesis and diversity of ribbing patterns in ammonites can be accounted for by the natural physical forces occurring at the tissue level during shell secretion. Our approach is to model the growth process in the simplest possible form that nevertheless still captures the essential mechanical features. The setup for the model is given schematically in Fig. 1(c) and (d). We work within a fixed circular geometry, with the shell radius given by $s(z)$, where z is the axial direction, i.e. the growth axis, and suppose the shell makes angle $\phi(z)$ with the z-axis. In this formulation, the shell is akin to a growing cone, and we will add the effect of shell coiling subsequently as a secondary effect. We model the mantle[1] and periostracum edges as circular elastic rings, each with reference stress-free radii dictated by the growth of the mollusk. That is, if the mantle/periostracum were removed from the shell, they would relax to a stress-free radius. The first key ingredient is that this radius may not coincide with the radius of the calcified shell, so that during growth the mantle and the periostracum are potentially stretched or compressed and can induce elastic forces.

As described above, during growth the mantle moves slightly beyond the shell edge and secretes the periostracum, which is then everted outside the mantle and serves as a connection between the mantle and the already calcified portion of the shell. This connecting region is the generative zone. This region provides the second key component to the morpho-mechanical model: the generative zone is pliable as it is yet to be calcified, but also forms a continuum with the rigid calcified portion of the shell, and thus acts somewhat like a torque spring, resisting a change in angle. That is, in the absence of any forces in the mantle/periostracum, the generative zone would maintain the same angle as the previously calcified portion of the shell edge to which it is attached, and work must be done to change the orientation.

The actual orientation of the generative zone and the radius of the newly secreted shell are thus determined by the balance of three forces: elastic forces in both the mantle and the periostracum, and a force in the generative zone. In a circular geometry, all forces are in the radial direction. First, we postulate the generative force

$$f_{GZ} = k_{GZ}\frac{d\phi}{dz}, \tag{1}$$

which characterises the resistance to change orientation, with k_{GZ} being a stiffness parameter. Next, we turn to the elastic forces in the mantle and the periostracum. In general, these would come from solving the equilibrium equations for two elastica, coupled via contact forces, and completed with constitutive laws relating stress to strain in each material. This computation is greatly simplified under two assumptions. First is the planar circular geometry already mentioned, in which case bending plays no role and the mechanics is purely governed by stretching/compressing, and second is the assumption that the mantle and the everted periostracum (hereafter denoted M/EP) are in perfect contact, a reasonable assumption given that the outer mantle lobe is fixed between the secreted, yet to be everted, and the already everted, portions of periostracum. Under the latter assumption, the two elastic rings are mechanically equivalent to a single elastic "bi-ring", characterised by an effective reference stress-free radius R and an effective stiffness K. These effective quantities are derived in Appendix G. The function $R = R(z)$ may be seen as a sort of average of the stress-free radii of the growing mantle and periostracum, and is thus dictated by the growth of the animal. For our purposes, we take the growth of the mollusc as given and compute the resulting form of the shell, thus $R(z)$ is taken as an input to the model.

We now compute mechanical equilibrium. Letting $r(z)$ be the radius of the M/EP in the current state, i.e. attached to the shell at point z along the growth axis, we define $\alpha = r/R$ as the stretch of the M/EP. Letting n denote the resultant tangential force in the M/EP, the radial force balance in the circular geometry gives (Moulton et al., 2012)

$$\frac{n}{R} + f_{GZ} = 0. \tag{2}$$

This is combined with a constitutive law for the effective single ring, given by $n = K(\alpha - 1)$. As shown in Appendix G, a simple linear relation exists between r and the shell radius s, that is $r = s - \beta$, where β is a typically small parameter that depends on the thickness and radii of the mantle and the periostracum. The stretch is thus given by $\alpha = (s - \beta)/R$ and we obtain the following differential equation for the angle $\phi(z)$:

$$\frac{d\phi}{dz} = \frac{k}{R(z)}\left(1 - \frac{s(z) - \beta}{R(z)}\right), \tag{3}$$

where $k = K/k_{GZ}$ characterises the relative stiffness of M/EP to generative zone. The system is completed with the geometrical relation

$$\frac{ds}{dz} = \tan\,\phi(z) \tag{4}$$

and conditions for the shell radius s and angle ϕ at a starting location denoted $z = 0$.

2.1. Summary

To summarise, we input to the model the mechanical properties of the mantle and the periostracum, the generative zone stiffness, and the growth of mantle and periostracum, i.e. radius and thickness as a function of shell length. From these we determine the single stiffness parameter k, the effective radius $R(z)$, and the parameter β. We then solve Eqs. (3) and (4), and output the shell radius $s(z)$ and orientation $\phi(z)$.

The function $R(z)$ is derived from a non-linear elastic force balance and is thus in general non-linear and the system must be solved by numerical means. However, as we show in Section 2.2, in many cases the system is well-approximated by a linear function and analytical progress may be made.

Base values for parameters are given in Appendix F. Thickness and mechanical parameters were estimated from the literature, under the assumption that Young's moduli and the relative thickness of mantle and periostracum do not vary greatly among mollusc species. The remaining parameter is the expansion rate of the mantle radius,[2] which in turns governs the gradient of the effective radius $R(z)$.

[1] For modelling purposes we only consider the edge of the outer mantle lobe, which for convenience we refer to as simply the mantle.

[2] The expansion rate of the periostracum is not independent of the mantle expansion.

2.2. Linearised theory

In this section we develop a linearised theory that yields an analytical solution to the system (3), (4). The complication in the system is the generally nonlinear function $R(z)$. However, if the mantle grows such that its stress-free radius and thickness are linear functions of z, and periostracum's stress-free state is dictated by that of the mantle (a natural assumption given that the periostracum is secreted in the mantle lobe), then R is itself well approximated by a linear function $R=R_0+\gamma z$, where γ is a dimensionless parameter describing the expansion rate of the stress-free periostracum radius and R_0 is an initial radius at starting point $z=0$ (see Appendix G). The generative zone stiffness k_{GZ} is very difficult to access with no measured values in the literature. We will make the assumption that the relative stiffness parameter k in (3) is approximately constant through development, which follows from the notion that the material stiffness of the M/EP increases in proportion with the stiffness of the generative zone. Finally, for material parameters typical of mantle and periostracum, the parameter β in (3) is of negligible size, and so $r\approx s$. Under these assumptions, the system becomes analytically tractable. We first scale the system by introducing the dimensionless parameters

$$z'=\frac{z}{L}+\frac{\xi}{\gamma},\quad R'=\frac{R}{R_0},\quad s'=\frac{s}{R_0}, \tag{5}$$

where L is a characteristic length for the shell and $\xi=R_0/L$. With the added shift in z', we have the convenient form $R'(z')=(\gamma/\xi)z'$. The system in dimensionless parameters is

$$\frac{ds'}{dz'}=\frac{1}{\xi}\tan\phi,\quad \frac{d\phi}{dz'}=\frac{k}{\xi R'}\left(1-\frac{s'}{R'}\right). \tag{6}$$

For initial conditions, we take $s(0)=R_0+\mu$, which in the scaled variables reads $s'(\xi/\gamma)=1+\epsilon$ with $\epsilon=\mu/R_0$ being a small parameter. We also assume that the initial shell orientation corresponds with the expansion rate, so that $\tan\phi(\xi/\gamma)=\gamma$. This choice is made for computational simplicity but a more generic choice has no significant effect on the results.

We seek a solution close to the linearly expanding stress-free M/EP by expanding as $s'=R'+\epsilon x$, $\phi=\phi_0+\epsilon\phi_1$, where ϕ_0 satisfies $\tan\phi_0=\gamma$. The problem at $O(\epsilon)$ reads

$$\frac{dx}{dz'}=\frac{1+\gamma^2}{\xi}\phi_1,\quad \frac{d\phi_1}{dz'}=\frac{-k\xi}{\gamma^2 z'^2}x. \tag{7}$$

This system can be solved exactly, yielding

$$x(z')=Az'^{1/2}\cos(\omega\ln z'-\nu) \tag{8}$$

with

$$\omega=\frac{\sqrt{4k(1+\gamma^2)-\gamma^2}}{2\gamma},\quad A=\sqrt{\frac{\gamma(1+4\omega^2)}{4\omega^2\xi}},$$
$$\nu=\omega\ln\frac{\xi}{\gamma}-\arctan\frac{1}{2\omega}. \tag{9}$$

An exact form for ϕ_1 can be determined from x via (7), but it is more useful to focus on the function $x(z')$. In Fig. 2 we present a comparison of the analytical solution $s'=R'+\epsilon x$ with x given by (8) with the full solution obtained by numerical integration. It is evident from (8) that ribbing naturally occurs in the system so long as the stress-free state of the mantle/periostracum does not perfectly coincide with the radius of the calcified shell, i.e. so long as $\epsilon\neq 0$. Any mismatch forces a change in orientation of the generative zone and creates an oscillatory component to the shell radius. Moreover, this mismatch is naturally induced in the system by the eversion of the periostracum (Appendix B).

In Fig. 2, the straight dashed green line is the effective radius $R(z)$. The shell radius oscillates about this growing stress-free state,

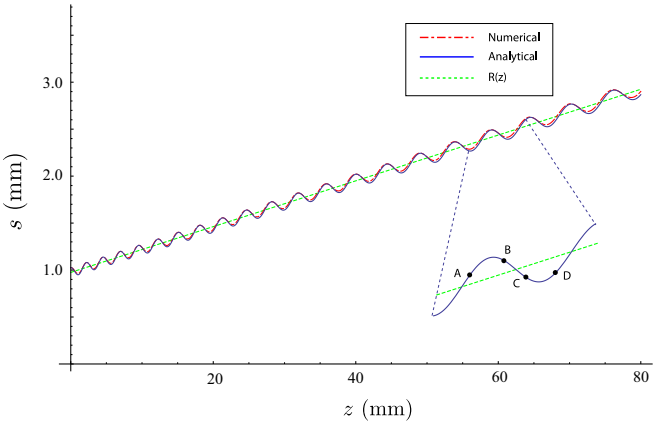

Fig. 2. Comparison of full numerical solution with the analytical solution. Inset: illustration of ribbing mechanism: shell radius oscillates about stress-free state of M/EP, passing from increasing tension while flaring out (A), decreasing tension (B) to increasing compression (C) during narrowing, to decreasing compression (D) and back to increasing tension. Mantle and periostracum stiffness parameters are as described in Appendix F, other parameters (see Appendix G): $k_{GZ}=0.03$, $\mu=0.05$, $M(0)=1$ mm, $\delta_M(0)=0.03$ mm, $\delta_P(0)=0.001$ mm, $\gamma=0.024$. (For interpretation of the references to colour in this figure caption, the reader is referred to the web version of this paper.)

and the general mechanism for rib formation can be summarised as follows:

1. Periostracum eversion creates a mismatch between the shell radius and the stress-free radius of M/EP.
2. When the generative zone is orientated outward and the shell radius is expanding, the M/EP will be subject to an increasing tension (point A in Fig. 2).
3. The build-up of tension eventually changes the orientation of generative zone from $\phi>0$ (flaring outward, radius increasing) to $\phi<0$ (narrowing, radius decreasing) (point B).
4. The tension is relieved but the orientation remains inward as compression starts to build up in the M/EP (point C).
5. Once enough compressive stress builds up, the orientation is converted back to outward (point D), and the cycle repeats.

We note that this general mechanism is consistent with the presence in intercostal valleys (i.e. toward points C and D) of compressive wrinkles seen on the outer shell surface of well preserved ammonites and corresponding to imprints in the calcified shell of wrinkling in the periostracum (Checa, 1994).

3. Results

We have shown that the morpho-mechanical model naturally produces an oscillatory pattern in the shell radius. We now seek to quantify and validate the predicted pattern against actual ammonite shells, and examine the diversity of ribbing in light of the mechanical model for morphogenesis.

3.1. Rib count

In the linearised model, the characteristics of the ribbing pattern can be understood in terms of two free parameters: the species dependent elastic parameter k controlling the effective material response of the tissue, and the specimen dependent expansion growth parameter γ characterising the linear expansion rate of a given shell. Assuming that the elastic parameter is constant across different specimens within a species, the ribbing pattern depends only on the expansion rate. As a test of the model,

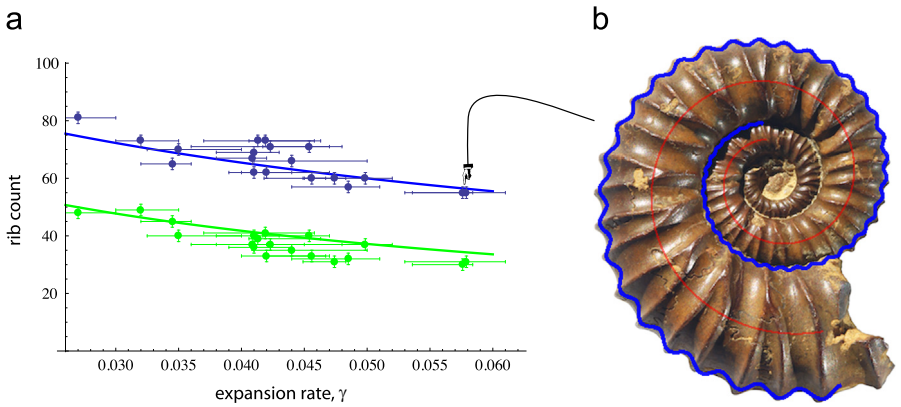

Fig. 3. Quantitative analysis of rib count and form. (a) Rib count data for ventral (blue) and dorsal (green) sides of 17 specimens of *Peltoceras schroederi*. The solid curves are the predicted rib counts from the theory, using a least-squares fitting for the single elastic parameter. (b) Theoretical rib profile overlaid on a shell, corresponding to the indicated data point. (For interpretation of the references to colour in this figure caption, the reader is referred to the web version of this paper.)

and to understand the effect of the expansion rate, we performed a detailed study of 17 specimens of *Peltoceras schroederi*. This species is particularly attractive to test the model, as they are well-approximated by a circular cross-section and also exhibit a strong intraspecific variation in expansion rate. On each specimen, we determined γ by fitting logarithmic spirals to high-resolution photographs of shells. We then manually counted the number of ribs on the ventral and dorsal sides produced over a particular shell length (Appendix D). In this way, for each specimen we extracted the number of ventral ribs, the number of dorsal ribs, and the expansion rate as shown in Fig. 3(a).

On the theoretical side, for given values of γ and k, the output of the model is the oscillating radius of a growing cone, and so to compare with the measured shells, we must include the effect of shell coiling. Details are given in Appendix A – the basic idea is to map the shell length variable z to the arclength of 3 separate logarithmic spirals, one for the centreline of the shell and one for each of the ventral and dorsal sides. The difference between ventral and dorsal sides is then interpreted as a difference in shell length in the mechanical model.

Using the linearised theory, we can determine the number of oscillations over a given shell length via the argument in the cosine in Eq. ((8)) (see Appendix C). Hence, for a given value of k, we can plot the predicted number of ribs over a particular length of shell as a function of the expansion rate γ. Since the length differential between the dorsal and ventral sides can be determined from the expansion rate, the theory can produce both a ventral and dorsal rib count as functions of γ, with only a single unknown parameter in the process, the relative stiffness parameter k. We then fit the two theoretical curves to the measured data from the 17 shells, with a least squares approximation used to determine the best fit value of k. The result appears in Fig. 3(a), where the solid curves are the predicted ventral (upper blue curve) and dorsal (lower green curve) rib counts.

That the model captures well the difference in rib count between the dorsal and ventral sides suggests that rib-splitting or intercalated ribs may be a simple consequence of the length differential between the ventral and dorsal sides of the shell. We note, however, that our model is not well suited to describe the actual splitting point of the ribs, as this by necessity requires a deviation from a circular cross-section. It seems likely that this can be understood within the same basic mechanical framework, but we leave this point as an interesting question for a future study.

To visually compare the predictions of the model, in Fig. 3 (b) we have taken the theoretical output for the ventral ribbing profile using the least squares value of k and a value of γ corresponding to the shell with the indicated data point in (a), and overlaid the ribbing pattern on the shell, demonstrating a remarkable agreement with the pattern predicted by the mechanical model.

3.2. Ribbing profile

We next examine the form of the ribbing profile. Some shells display a nearly sinusoidal profile, which can be understood as a consequence of a symmetric elastic response of the mantle/periostracum to tension versus compression. This is the shape predicted by Eq. (8), and as indicated in Fig. 3(b), produces a reasonable fit in some cases. However, many shells have a marked asymmetry in their profile, exhibiting a ribbing pattern with wide valleys and sharp ridges. A comprehensive review of the literature as well as a consultation with the two main collections of France (Paris museum, and Lyon university) reveals that some asymmetry is quite generic in the sense that in a direct examination of 1100 out of about 1500 known Jurassic and Cretaceous genera, at least 800 genera present a definite asymmetry where ridges have greater curvature than valleys.

This asymmetry can be understood mechanically as an asymmetric response to tension version compression, which is a common feature in thin biological materials (Cardamone et al., 2009; Guthardt Torres, 2012). Such asymmetry can be easily incorporated in the mechanical model by utilising a bimodular elastic response, that is we define a different elastic parameter for compression than for tension, so that in Eq. (3) we write

$$k = \begin{cases} k_c & \text{if } \alpha < 1 (\text{compression}) \\ k_t & \text{if } \alpha > 1 (\text{tension}). \end{cases} \tag{10}$$

With asymmetry introduced, the ribbing profile is also strongly affected by the degree of initial mismatch, i.e. the value $\epsilon = \mu/R_0$ in the initial condition $R = R_0 + \mu$. In Fig. 4, we plot ribbing profiles over a short length of shell for different values of k_t and k_c and varying ϵ, obtained by numerically integrating the system (3), (4) with linear function $R = R_0 + \gamma z$ and piecewise constant k given by (10). We observe a diversity of profiles, qualitatively representative of the morphological diversity in ammonites.

3.3. Ribbing wavelength and amplitude

We next examine trends in the amplitude and wavelength of ribbing. More than a century ago, Buckman (1887) noted in a Jurassic species displaying high variability that inclusion and compression of whorls correlate with the degree of ornamentation, an observation since then made in many distantly related

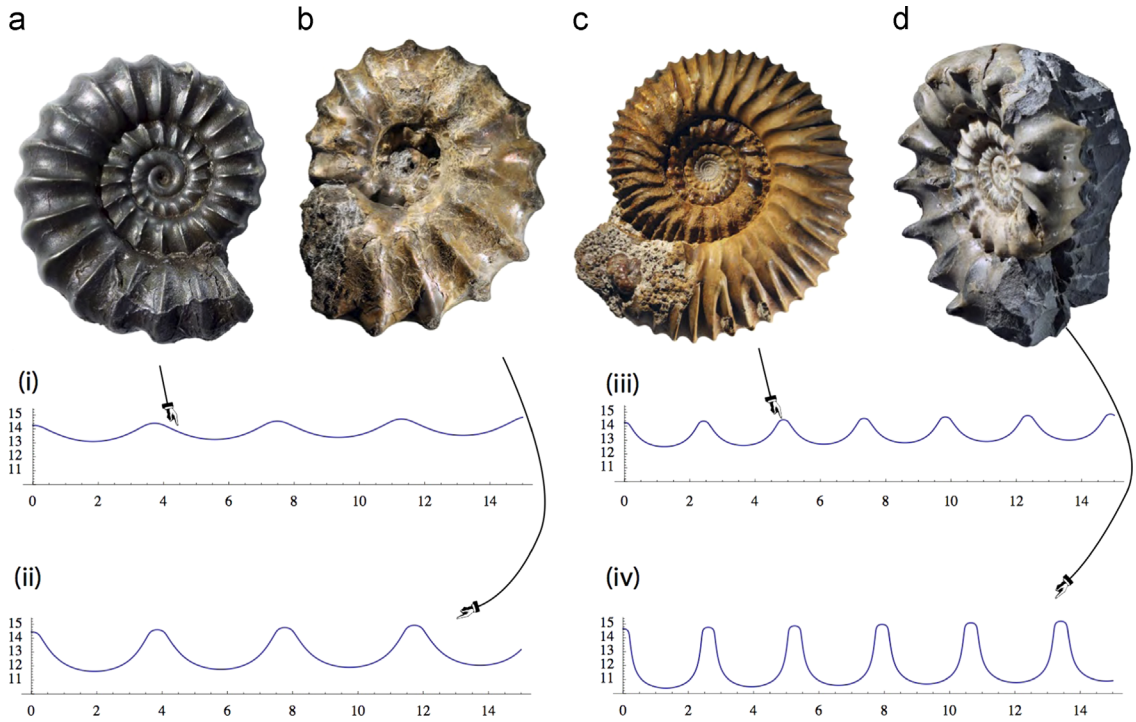

Fig. 4. Asymmetric ribbing profiles. Shells are (a) *Promicroceras*, (b) *Protohoplites* (c) *Stephanoceras*, (d) *Xipheroceras*. Asymmetry arises in model from bimodular elastic response to tension/compression. Stiffness parameters and initial mismatch ϵ in simulated profiles: (i) $k_t=900$, $k_c=60$, $\epsilon=0.018$, (ii) $k_t=900$, $k_c=30$, $\epsilon=0.032$, (iii) $k_t=1300$, $k_c=90$, $\epsilon=0.024$, (vi) $k_t=950$, $k_c=30$, $\epsilon=0.046$; other parameters are same for all cases: $\gamma=0.04$, $R_0=14$.

species (Westermann, 1966; Kennedy and Cobban, 1976; Dagys and Weitschat, 1993; Weitschat, 2008; Hammer and Bucher, 2006), and during the evolution of lineages as well (Bayer and McGhee, 1984). In our terminology, this so-called Buckman's law of covariation states that the magnitude of ribbing is positively correlated with the shell cross-sectional curvature. A covariation between curvature and ribbing pattern is also evident as a general trend that can be seen in the classic Raup morphospace (Raup, 1967), Fig. 5(a), in which shell forms are characterised by an expansion rate parameter W and a parameter D related to the tightness of coiling. In the upper right of the diagram are shells with low expansion rate and thus a small rate of decrease of curvature of shell cross-section – these shells typically have dense ornamentation. In the lower left of the diagram are shells with high expansion rate (large rate of decrease of curvature) – these shells have almost no ornamentation, appearing smooth or almost smooth. Between these extremes are shells with moderate expansion rate and a coarse ornamentation. Ammonoid and Nautiloid distributions in the morphospace are indicated by the blue and red regions, respectively; evolutionary trends are indicated by the blue arrows, showing a general trend toward smoother shells; and the brown, blue, and green lines correspond to published examples of Buckman's law of covariation, displaying the wide spectrum of coiling variability (Kennedy and Cobban, 1976; Dagys and Weitschat, 1993; Weitschat, 2008; Hammer and Bucher, 2006).

To see whether this trend can be understood in the framework of our model, we simulated three shells with different expansion and coiling parameters that can be mapped to exact points in each of the regions of Raup's morphospace, and with all other parameters equal, to see how the location in Raup's morphospace affects the emergent ribbing pattern. We solve the mechanical model using the best-fit stiffness parameter k as determined in Section 3.1, and with fixed initial conditions, while varying only the expansion rate γ. We then superpose the ribbing pattern on a parameterised planispiral shell that expands with rate γ. To create the shell, we take a logarithmic spiral as a centreline curve, i.e. the polar equation $\rho=ae^{b\theta}$, where the exponent b dictates the tightness of the spiral. At each point on the centreline curve, we construct the shell by attaching a circle in the plane normal to the tangent direction, whose radius is the solution of the mechanical model. The two independent coiling and expansion parameters can be mapped directly to Raup's D and W parameters (Appendix E), so that each simulated shell can be placed exactly on Raup's diagram but are otherwise identically produced with equivalent initial conditions and mechanical properties.

The result is illustrated in Fig. 5(b)–(d); the model precisely predicts the observed trend from dense to coarse to smooth shell. While it is likely that "initial conditions" and other mechanical parameters are not exactly equal between the Ammonoids in the upper right of the diagram and the Nautiloids in the lower left, we note that the trend is captured nonetheless and thus might be understood fully in mechanical terms. Effectively, the high expansion rate of the simulated nautiloid serves to damp out the oscillations that remain prominent in the shell with low expansion rate.

To investigate this relationship further, we can use the linearised theory to obtain explicit mathematical relationships. In particular, several scaling relations may be inferred from the form of the exact solution (8) of the linearised system. Within the development of an individual shell, the parameters γ and k are fixed, and hence the amplitude of the ribbing pattern increases through development at a rate of shell length to the one half power, while the frequency of ribbing decreases logarithmically due to the $\ln z'$ term inside the cosine.

The decrease in frequency directly governs the number of ribs over a given length of shell (Fig. 3(a)). The increase in amplitude over the development of a given shell is more difficult to verify, since the absolute change in amplitude is small, and ribbing amplitude is less straightforward to measure and more prone to noise due to degradation of ribs. In Fig. 6, we have taken a *Peltoceras schroederi* specimen with particularly well-preserved ribs, measured the amplitude of the ribs on the outside whorl, and

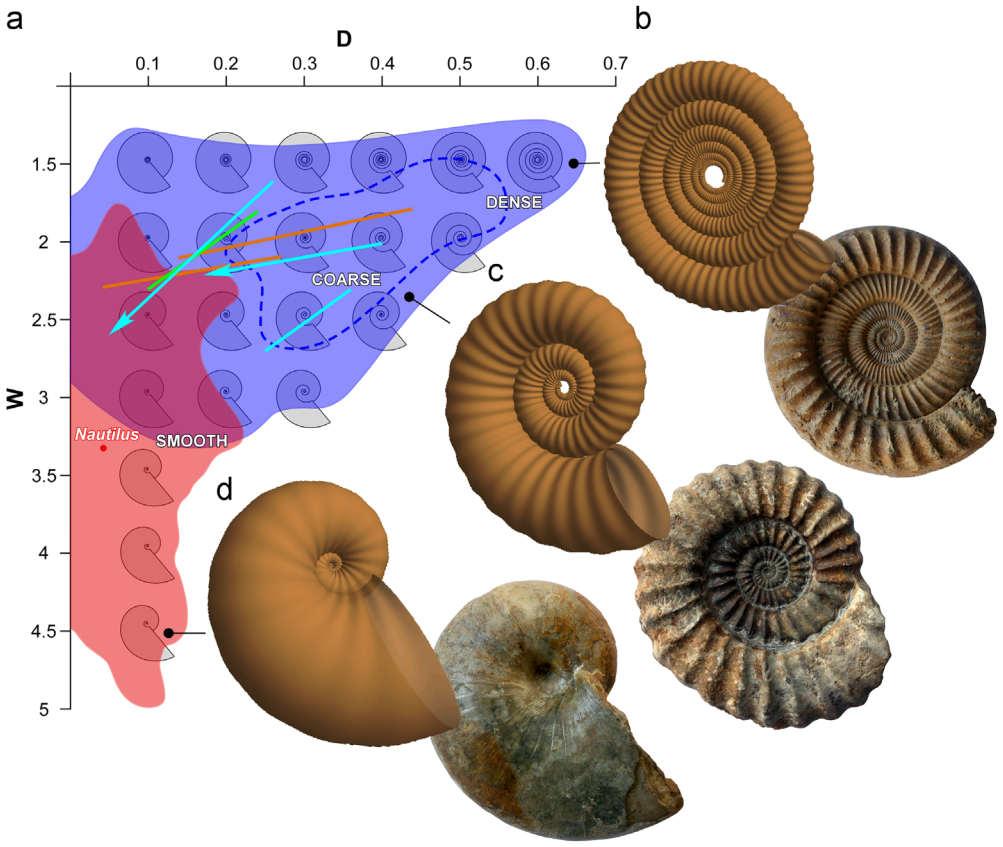

Fig. 5. Ribbing pattern and evolutionary trends in morphospace. (a) Ammonoid (blue zone) and Nautiloid (red zone) distribution in the Raup morphospace (Raup, 1967; Ward, 1980). Dashed blue line: distribution of highly ornamented ammonites (Raup, 1967). Blue arrows: evolutionary trends from strongly ornamented to smooth shells in Jurassic lineages (Bayer and McGhee, 1984). The brown, blue and green lines represent the spectrum of shell coiling variability in not closely related Triassic, Jurassic and Cretaceous species displaying the Buckman's law of covariation (data from: Kennedy and Cobban, 1976; Dagys and Weitschat, 1993; Weitschat, 2008; Hammer and Bucher, 2006).(b)–(d) Simulated shells at values (b): $D=0.65, W=1.5$, (c): $D=0.42, W=2.4$, (d): $D=0.13, W=4.5$. All other parameters are equivalent in each shell, and are provided in Appendix F. The shells are: (b) *Perisphinctes*, an ammonite (c) *Aegoceras*, an ammonite and (d) *Cenoceras*, a nautilid. (For interpretation of the references to colour in this figure caption, the reader is referred to the web version of this paper.)

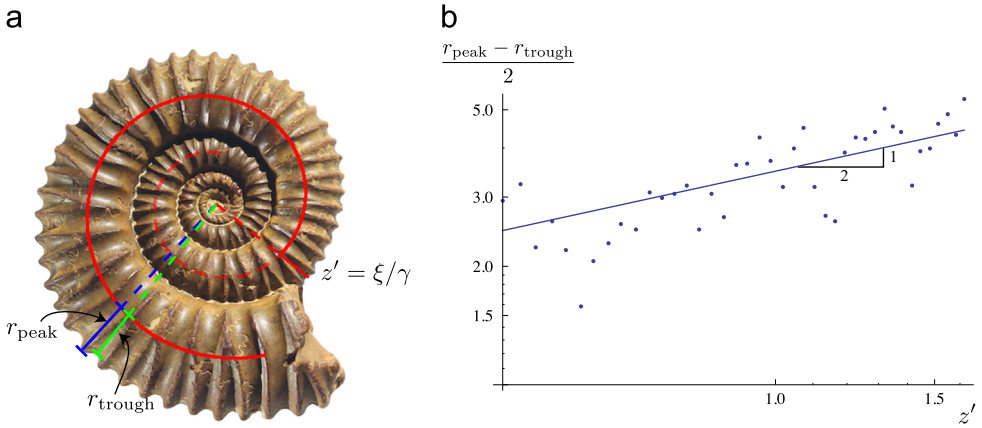

Fig. 6. Amplitude scaling law. (a) The amplitude is computed by the difference in distance between the shell centreline and the peaks and troughs of each rib, as a function of arclength of centreline form starting point $z' = \xi/\gamma$. (b) Amplitude plotted against shell arclength on a log–log scale. Solid line has slope 1/2 predicted by the theory.

plotted the amplitude against the scaled length z' on a log–log plot. The straight line is the predicted scaling law, with slope 1/2.

To compare ribbing pattern between individuals, we examine the form of the prefactor terms A and ω, for the amplitude and frequency, respectively. In particular, we consider the dependence of these terms on the most easily identifiable and comparable variable between shells, the expansion rate γ. For a typical shell, $\gamma \ll 1$, and even in the rapidly expanding shell of Fig. 5(d), $\gamma \approx 0.18$. For small γ, A and ω scale as $A \sim \gamma^{1/2}$, $\omega \sim \gamma^{-1}$. Rather than frequency and absolute amplitude, better indicators of ribbing form are the relative ribbing amplitude, i.e. ribbing amplitude divided by shell radius, and ribbing wavelength. The relative ribbing amplitude a is determined by taking the absolute amplitude divided by radius $R' = \gamma z'$, and the wavelength λ scales as

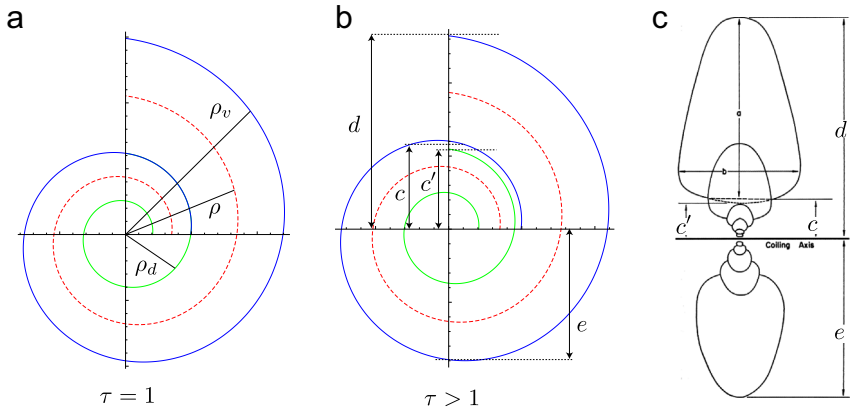

Fig. 7. Logarithmic spirals and Raup's parameters. (a) The logarithmic spirals representative of the shell centreline ρ, dorsal side ρ_d and ventral side ρ_v in the case of perfect contact between whorls, $\tau = 1$. (b) Raup's parameters labelled on a shell with overlap, $\tau > 1$. Note that the parameter c requires the geometry of the transverse direction, as this is the intersection point between whorls. (c) Parameters for Raup's morphospace, a reproduction of Fig. 1 from Raup (1967), with permission.

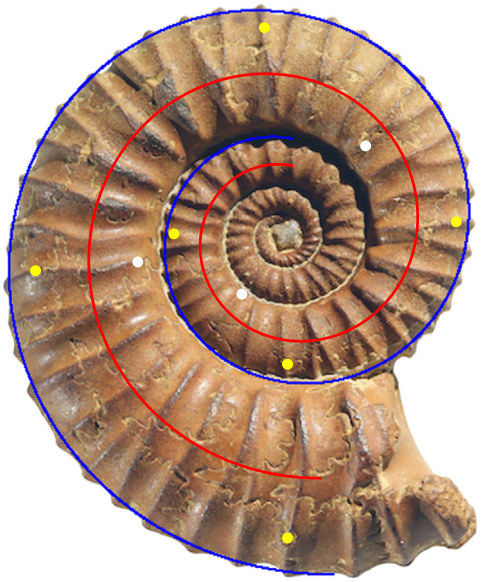

Fig. 8. Example of best fit spirals to shell image and rib counting. Yellow dots mark each 10th ventral rib; white dots mark each 10th dorsal rib. (For interpretation of the references to colour in this figure caption, the reader is referred to the web version of this paper.)

$1/\omega$. We thus obtain the scaling laws

$$a \sim \kappa^{1/2}, \quad \lambda \sim \kappa^{-1}. \tag{11}$$

This general relationship between ribbing pattern and curvature suggests that both the intraspecific variation in Buckman's law as well as the general evolutionary trend evident in Raup's diagram can be seen as the expression of a simple morphogenetic rule linked to constraints of curvature on growth mechanics that can be generalised to the case of non-circular cross-sections. Note also that some shells undergo allometric variation and their opening becomes more elliptical during development, marked by a nonlinear decrease in lateral curvature. This trend is associated with a nonlinear expansion rate within our modelling framework.

4. Discussion

The state of knowledge with ammonite shell form is one of many facts but few explanations. Over the last 2 centuries paleontologists have amassed a huge body of descriptive literature on ammonites and inferred their evolutionary history. Yet, the generative processes underlying their form and morphological diversity remained unknown. The morpho-mechanical model developed here provides the first quantitative explanation and theoretical framework through which these facts and observations may begin to be weaved into a consistent story. It also provides a new organising framework to study morphogenesis and evolutionary trends of the shells of other mollusks. As an immediate and significant instance of this, our approach sheds light on a long-standing puzzle of cephalopod evolution. *Nautilus* has long fascinated biologists and palaeontologists due to its morphological conservatism for which it has been called a "living fossil". This concept is misleading, however, as it has often been interpreted to imply a lack of evolutionary change, though recent molecular phylogeny suggests that the living *Nautilus* lineage is currently undergoing a period of evolutionary radiation masked by cryptic speciation (Bonacum et al., 2011). Unlike ammonites, which display great variation in shell coiling and ornamental patterns, nautilids have been restricted to a rapidly expanding shell coiling morphology since at least the early Jurassic (Ward, 1980) (Fig. 5(a)) and, consistent with our model, their shells have remained essentially smooth. Also consistent is the presence of strongly ornamented Palaeozoic and Triassic nautilids genera (e.g. *Tylonautilus*, *Pleuronautilus*, *Tainionautilus*) in regions of the Raup's morphospace occupied by strongly ornamented Jurassic and Cretaceous ammonites, but unoccupied by post-Triassic nautilids. These observations are all consistent with the simple explanation that since at least the early Jurassic, nautilids shells have had a very high expansion rate and thus, for purely mechanical reasons, have lacked the distinctive ornamental patterns that palaeontologists use to reconstruct phylogeny and to infer the evolution of diversity.

Acknowledgements

AG is a Wolfson/Royal Society Merit Award Holder; AG acknowledges support from EC Framework VII through a Reintegration Grant.

Appendix A. Coiling geometry

The mechanical model we have developed treats the shell as a growing cone. To make comparisons with shells, and to determine coiling and expansion properties, we now include shell coiling. The starting point is to assume that the centreline of the shell follows a logarithmic spiral. That is, we describe the centreline in polar coordinates by $\rho = ae^{b\theta}$, where ρ is the radius as measured from the centre of the shell, θ is the polar angle, and a and b are constants. The dorsal and ventral sides also follow logarithmic

spirals ρ_d and ρ_v, given by $\rho_d=(a-R_0)e^{b\theta}$, $\rho_v=(a+R_0)e^{b\theta}$, where R_0 is the initial shell radius, and $\theta=0$ is defined by the starting location on the shell. As before, we scale the radii by R_0 and introduce the dimensionless parameter $\eta=a/R_0$ so that the dimensionless centre, dorsal, and ventral spirals satisfy

$$\rho'=\eta e^{b\theta},\quad \rho'_d=(\eta-1)e^{b\theta},\quad \rho'_v=(\eta+1)e^{b\theta}. \tag{A.1}$$

Next, we identify the parameter z in the mechanics model with the arc length of the centreline, that is

$$z(\theta)=\int_0^\theta \sqrt{\rho^2+\frac{d\rho^2}{d\theta}}\,d\theta,$$

from which we obtain the dimensionless length

$$z'(\theta)=\xi\frac{\eta\sqrt{1+b^2}}{b}\left(e^{b\theta}-1\right)+\frac{\xi}{\gamma}. \tag{A.2}$$

The dorsal and ventral lengths have similar expressions, but with η replaced by $\eta-1$ in the dorsal case and $\eta+1$ in the ventral case. From (A.2), the stress-free shell radius is given as a function of θ by $R'(\theta)=(\gamma/\xi)z'(\theta)$. The ventral and dorsal spirals are related through the tightness of the coiling. This is imposed through the relation $\rho'_v(\theta)=\tau\rho'_d(\theta+2\pi)$, where the parameter τ describes the amount of gap or overlap between whorls. Specifically, $\tau=1$ corresponds to perfect contact, $\tau>1$ implies an overlap, while $\tau<1$ implies a gap between the dorsal side of the shell and the ventral side of the preceding whorl (Fig. 7(a), (b)). We assume that τ is a fixed parameter for a given shell, and thus find

$$e^{2\pi b}=\frac{\eta+1}{\tau(\eta-1)}. \tag{A.3}$$

It remains to relate the ventral and centre spirals through the expansion of the shell. Setting $\rho_v(\theta)=\rho(\theta)+R'(z'(\theta))$, we obtain

$$\frac{\gamma\eta\sqrt{1+b^2}}{b}=1. \tag{A.4}$$

Eqs. (A.3) and (A.4) may be thought of as setting two of the shell geometry parameters $\{a,R_0,b,\tau\}$.

Appendix B. On periostracum eversion

Note that in the model formulation, a solution exists for which no oscillations occur. Namely, if the initial radius exactly matches the shell radius and the initial orientation matches the gradient caused by the expansion rate, then the solution to the linearised problem is $x\equiv 0$, i.e. no ribbing forms. However, due to the eversion of the periostracum, such initial conditions will not occur. In particular, consider the situation where at a given starting point the mantle is completely stress-free and the shell orientation exactly matches the expansion gradient. This situation is not mechanically stable, as the periostracum will also be stress-free *before* eversion, but both mantle and periostracum cannot be stress-free after eversion. Thus, the stress-free state of the M/EP will not exactly coincide with the shell radius, and thus the starting conditions will induce oscillations.

The amplitude of oscillations, i.e. magnitude of ribs, is closely linked to this mismatch in M/EP. That is, the constant μ in the condition $s(0)=R_0+\mu$ is linked to the mismatch, and is in turn linked to the thickness of mantle and periostracum. Thus if, for instance, the thickness of outer mantle lobe is very small, the value of μ would be smaller and we would expect a smaller ribbing amplitude. Since initial mismatches and initial orientations are very difficult to gauge from one shell to another, we have kept a constant value for $\epsilon=\mu/R_0$.

Appendix C. Rib count

The number of ribs in a given segment of shell predicted by the model is determined by the number of oscillations of $\cos(\omega\ln z'-\nu)$ for $z'\in[\xi/\gamma,1+\xi/\gamma]$. This count is made more convenient by defining $\hat{z}=z'-\xi/\gamma$. Then, defining the function $f(\hat{z},\gamma;\xi)=\omega\ln(\hat{z}+\xi/\gamma)-\nu$, the number of ribs (as a continuous value, not integer) predicted along the centreline spiral is

$$n(\gamma)=\frac{f(1,\gamma;\xi)}{2\pi}. \tag{C.1}$$

To compute the number of ribs on the ventral and dorsal sides, we only apply the same formula, but with a different total length. As $\hat{z}$ runs from 0 to 1, the lengths along the ventral and dorsal sides are, respectively, $l_v=(\eta+1)/\eta$, $l_d=(\eta-1)/\eta$, and thus the rib count on ventral and dorsal sides are

$$n_v(\gamma)=\frac{f(l_v,\gamma;\xi)}{2\pi},\quad n_d(\gamma)=\frac{f(l_d,\gamma;\xi)}{2\pi}. \tag{C.2}$$

Appendix D. Shell fitting

In order to compare the model predictions of ribbing pattern with shell specimens, we first loaded an image of each shell into Mathematica®. In view of Eqs. (A.3) and (A.4), which give the parameters b and γ in terms of η, the three spirals depend on three parameters: a, R_0, and the overlap parameter τ (which for the *Peltoceras schroederi* specimens was approximately one). We thus varied the two parameters a and R_0 until the centre and dorsal spirals reached a visual best overlay. In the simplified linear model, the ribbing pattern depends on three dimensionless parameters. One is $\xi=R_0/L$, the initial radius to length ratio. For all specimens, we fixed $\xi=0.02$, which may be thought of as setting the length of shell to be considered as a function of its starting radius R_0. The second is the expansion rate γ, which is determined for each specimen as outlined above. The third is the mechanical parameter k. This parameter cannot be measured from the images, and although the material stiffness of mantle and periostracum can be inferred from the literature, the amount of variation between species is uncertain; moreover, no data exists on the generative zone stiffness k_{GZ}. Thus, our approach is to assume that for a given species, the effective mechanical parameter k is approximately constant, and we determine this single parameter by fitting the model predictions of rib count to the shell data.

For each shell, once the best fit spirals have been determined, the fixed value of ξ determines the length of the shell segment. Over that length of shell, we counted manually the number of ribs on the ventral and dorsal sides (Fig. 8). For each shell we measured an expansion rate γ, a dorsal rib count, and a ventral rib count. In Fig. 2(a) of main text these data are compared against the model predictions as given by formulas (C.2). We determined k to be the value for which the model prediction best fit the data curves, through a least squares analysis, obtaining $k=154.75$. We then directly compared the ribbing pattern prediction by adding the oscillations predicted by the model with $k=154.75$ to the logarithmic spirals, and overlaying the curve on the image of the shell (Fig. 2(b)).

Appendix E. Raup's morphospace

Numerous evolutionary trends can be observed in terms of shell variation in the classic Raup morphospace (Raup, 1967). To test our hypothesis that variations in ribbing pattern seen in different regions of the morphospace can be understood as mechanical effects of expansion rate, we need to map our coiling

parameters to the two morphospace parameters, D and W. The conversion is illustrated in Fig. 7: Raup's diagram is reproduced in Fig. 7(c), with the equivalent parameters labelled on our logarithmic spirals in Fig. 7(b). Specifically, we find

$$W = \left(\frac{d}{e}\right)^2 = \left(\frac{\rho_v(\theta)}{\rho_v(\theta-\pi)}\right)^2. \tag{E.1}$$

The computation for Raup's D is slightly more complex, since $c = c'$ only if there is perfect overlap, i.e. $\tau = 1$. If $\tau = 1$, $c = \rho_d$ and we obtain the simple formula

$$D = \frac{c}{d} = \frac{\rho_d(\theta)}{\rho_v(\theta)}. \tag{E.2}$$

When overlap is included, a straightforward geometrical calculation gives

$$c = \rho(\theta - 2\pi) + \frac{1}{2}\left(B - \frac{a^2 - a'^2}{B}\right)$$

where $B = \rho(\theta) - \rho(\theta - 2\pi)$, $a = R(\theta)$, $a' = R(\theta - 2\pi)$.

In creating the 3D simulated shells in Fig. 4, we have used the coiling parameters (b) $a = 40$, $R_0 = 8.3$, $\tau = 1.03$ (c) $a = 26$, $R_0 = 10.6$, $\tau = 1$ (d) $a = 16.87$, $R_0 = 13.2$, $\tau = 1.74$, which translates to Raup's parameters (b) $D = 0.65$, $W = 1.5$, (c) $D = 0.42$, $W = 2.4$, (d) $D = 0.13$, $W = 4.5$. Ribbing parameters were the same in all cases: $\xi = 0.02$, $k = 155$, $\epsilon = 0.1$.

Appendix F. Parameters

We have used the following parameters as base values for mechanical properties and dimensions. We use for the mantle Young's modulus $E_M = 0.8$ MPa, based on measurements of squid mantles (Macgillivray et al., 1999). The periostracum is significantly stiffer, with Young's modulus on the order of $E_P = 100$ MPa, based on measurements of mussels (Waite et al., 2002). We infer base values for mantle and periostracum thickness based on measurements of *Nautilus*. From images of embryonic *Nautilus* (Mutvei et al., 1993), the outer mantle lobe is approximately 150 μm thick, while the periostracum has thickness on the order of 1 μm. From images by Westermann et al. (2005) on juvenile *Nautilus*, the outer mantle is between 400 and 700 μm thick, with periostracum thickness 3–5 μm. Shell radii can vary dramatically between species and over the development of the shell. We use as base values approximate measurements from images of *Peltoceras schroederi*, in which the shell radius increases from around 1 mm to 3–5 mm over a length of shell between 40 and 100 mm. Finally, note that we have formulated a continuous, quasistatic growth process. The quasistatic assumption follows naturally from the fact that growth occurs on a much slower time scale than the elastic time scale, so the system is always assumed to be in mechanical equilibrium. Regarding the assumption on continuous growth: while it is commonly understood that shell growth occurs in discrete steps of secretions, these steps are so small that they can naturally be described as a continuous process.

Appendix G. Mantle/everted periostracum elastic ring

Here we characterise the mechanical properties of the mantle/everted periostracum. Let $M = M(z)$ be the stress-free mantle radius,[3] and $\delta(z)$ be the combined half-thickness of mantle and periostracum. Then the periostracum, secreted inside the periostracal groove, has stress-free radius $P = M - \delta$. In the deformed state, i.e. attached to the shell edge, let $m(z)$ and $p(z)$ be the radii of mantle and periostracum, respectively, and note the relation $p = m + \delta$, which reflects the eversion of the periostracum.

Assuming perfect contact between mantle and everted periostracum, mechanically the mantle/everted periostracum (M/EP) acts as a single circular elastic rod, whose properties derive from the mantle and the periostracum. Once we have characterised the mechanical properties of the M/EP, the problem is equivalent to the deformation of an elastic ring under a radial force, here the generative zone force.

Mechanical equilibrium for an elastic ring is determined through the standard Kirchhoff equations for an elastic rod, here within a fixed circular geometry. The balance of linear momentum for an elastic rod reads (Antman, 2006) $\mathbf{n}'(S) + \mathbf{f} = \mathbf{0}$, where $\mathbf{n}$ is the resultant force attained by averaging the stresses over a cross-section, S is the reference arclength, and $\mathbf{f}$ is an external body force per unit reference length. For a fixed circular geometry, the mechanics is fully governed by stretching; that is when a ring deforms to a ring of a different size, there is no change in the bending energy, only the stretching energy. Hence the only non-vanishing component of $\mathbf{n}$ is along the tangent direction, i.e. the stretching/compression force. Thus we can write $\mathbf{n} = n\mathbf{e}_\theta$, where $\mathbf{e}_\theta$ is the circumferential unit vector. We assume $\mathbf{f}$ acts in the radial direction and has the general form $\mathbf{f} = f(r, dr/dz, \ldots)\mathbf{e}_r$, where r is the radius in the deformed state and $\mathbf{e}_r$ is the radial unit vector. Using

$$\frac{d\mathbf{e}_\theta}{dS} = \frac{\mathbf{e}_r}{R},$$

where R is the reference radius of the elastic ring, the balance of linear momentum in the radial direction then takes the simple form

$$\frac{n}{R} + f = 0. \tag{G.1}$$

The system is completed by a constitutive law relating the force n to the elastic stretch

$$\alpha = \frac{r}{R}.$$

Here we consider a linear relation,

$$n = K(\alpha - 1), \tag{G.2}$$

where K is the elastic (stretching) stiffness. Substituting (G.2) into (G.1) gives a single equation for mechanical equilibrium:

$$\frac{K}{R}\left(\frac{r}{R} - 1\right) + f = 0. \tag{G.3}$$

Eq. (G.3) fully describes the mechanics of a deformed elastic ring. For the M/EP system, $f = f_{GZ}$ (Methods, Eq. (1)), and we just need to characterise the radii r and R and the stiffness coefficient K in terms of the growing mantle and periostracum. Let n_M, n_P be the tangential resultant forces for mantle and periostracum, respectively, satisfying linear constitutive laws:

$$\begin{aligned} n_M &= K_M(\alpha_M - 1) \\ n_P &= K_P(\alpha_P - 1), \end{aligned} \tag{G.4}$$

where $\alpha_{M,P}$ are the elastic stretch of mantle and periostracum, given by

$$\alpha_M = \frac{m}{M}, \quad \alpha_P = \frac{p}{P},$$

and the elastic stiffnesses satisfy

$$K_M = E_M \delta_M w, \quad K_P = E_P \delta_P w.$$

Here $E_{M,P}$ are the respective Youngs moduli, δ_M and δ_P are the half-thicknesses of mantle and periostracum, respectively (so $\delta = \delta_M + \delta_P$), and w is the transverse width of the mantle edge/periostracum. Extending work on growing elastic rings

[3] We assume radius is measured to the centreline of the ring.

(Moulton et al., 2012)[4] to a pair of rings, the elastic stiffness of the M/EP birod is given by the relation

$$K = K_M + K_P,$$

and the reference radius satisfies

$$R = P \cdot \frac{g(1+\kappa)}{\kappa+g}, \tag{G.5}$$

where $g = M/P$ and $\kappa = K_M/K_P$. If the mantle and the periostracum thicknesses increase in proportion with their radii, then the term multiplying P in (G.5) is constant, close to unity. Since the periostracum is much stiffer than the mantle, κ is a small parameter. Finally, we have the following relation between the radius r of the M/EP and the radius p of the everted periostracum:

$$r = p - \frac{\delta\kappa}{g+\kappa}, \tag{G.6}$$

In the current state, since shell secretion occurs at the periostracum, we set the shell radius equal to the everted periostracum, i.e. $s = p$, and note that (G.6) defines the parameter β as

$$\beta := \frac{\delta\kappa}{g+\kappa}. \tag{G.7}$$

For typical parameters β is of order 10^{-2} and the M/EP radius approximately equals that of the everted periostracum.

References

Antman, S., 2006. Nonlinear Problems of Elasticity. Springer, New York, NY.

Bayer, U., McGhee, G.R., 1984. Iterative evolution of middle jurassic ammonite faunas. Lethaia 17 (1), 1–16.

Bonacum, J., Landman, N.H., Mapes, R.H., White, M.M., White, A.-J., Irlam, J., 2011. Evolutionary radiation of present-day *Nautilus and Allonautilus*. Am. Malacol. Bull 29, 77–93.

Brayard, A., Escarguel, G., Bucher, H., Monnet, C., Bruehwiler, T., Goudemand, N., et al., 2009. Good genes and good luck: ammonoid diversity and the end-permian mass extinction. Science 325 (5944), 1118–1121.

Buckman, S.S., 1887. A Monograph of the Inferior Oolite Ammonites of the British Isles. Palaeontographical Society, London.

Cardamone, L., Valentín, A., Eberth, J.F., Humphrey, J.D., 2009. Origin of axial prestretch and residual stress in arteries. Biomech. Model. Mechanobiol. 8 (January (6)), 431–446.

Chamberlain Jr, J.A., Westermann, G., 1976. Hydrodynamic properties of cephalopod shell ornament. Paleobiology, 316–331.

Checa, A., 1994. A model for the morphogenesis of ribs in ammonites inferred from associated microsculptures. Palaeontology 37 (4), 863–888.

Chirat, R., Moulton, D.E., Goriely, A., 2013. Mechanical basis of morphogenesis and convergent evolution of spiny seashells. Proc. Natl. Acad. Sci. U. S. A. 110 (15), 6015–6020.

Cowen, R., Gertman, R., Wiggett, G., 1973. Camouflage patterns in nautilus, and their implications for cephalopod paleobiology. Lethaia 6 (2), 201–213.

Dagys, A.S., Weitschat, W., 1993. Extensive intraspecific variation in a triassic ammonoid from Siberia. Lethaia 26 (2), 113–121.

Eldredge, N., 1996. Ammonoids do it all. In: Landman, N.H., Tanabe, K., Davis, R.A. (Eds.), Ammonoid Paleobiology. Plenum Press, New York.

Gould, S.J., 2002. The Structure of Evolutionary Theory. Harvard University Press, Cambridge, MA.

Guthardt Torres, 2012. Contractile network models for adherent cells. Phys. Rev. E 85 (January (1)), 011913.

Hammer, Ø., 2000. A theory for the formation of commarginal ribs in mollusc shells by regulative oscillation. J. Molluscan Stud. 66 (3), 383.

Hammer, Ø., Bucher, H., 2006. Generalized ammonoid hydrostatics modelling, with application to Intornites and intraspecific variation in Amaltheus. Paleontol. Res. 10 (1), 91.

Hutson, M.S., Ma, X., 2008. Mechanical aspects of developmental biology: perspectives on growth and form in the post-genomic age. Phys. Biol. 5 (1), 015001.

Kennedy, W.J., Cobban, W.A., 1976. Aspects of Ammonite Biology, Biogeography, and Biostratigraphy.

Macgillivray, P.S., Anderson, E.J., Wright, G.M., Demont, M.E., 1999. Structure and mechanics of the squid mantle. J. Exp. Biol. 202 (6), 683–695.

Meinhardt, H., 2009. The Algorithmic Beauty of Sea Shells, 4th ed. Springer Verlag, Heidelberg.

Moulton, D.E., Lessinnes, T., Goriely, A., 2012. Morphoelastic rods. Part 1: a single growing elastic rod. J. Mech. Phys. Solids 61 (2), 398–427.

Mutvei, H., Arnold, J.M., Landman, N.H., 1993. Muscles and attachment of the body to the shell in embryos and adults of *Nautilus belauensis* (Cephalopoda). Am. Mus. Novit. 3059.

Raup, D.M., 1967. Geometric analysis of shell coiling: coiling in ammonoids. J. Paleontol., 43–65.

Saleuddin, A.S.M., Petit, H.P., 1983. The mode of formation and the structure of the periostracum. In: Saleuddin, A.S.M., Wilbur, K.M. (Eds.), The Mollusca, Physiology. Academic Press, New York, pp. 199–233.

Simkiss, K., Wilbur, K.M., 1989. Biomineralization. Academic Press, New York.

Vermeij, G.J., 1993. Evolution and Escalation. An Ecological History of Life. Princeton University Press, Princeton, NJ.

Waite, J.H., 1983. Quinone-tanned scleroproteins. In: Saleuddin, A.S.M., Wilbur, K. M. (Eds.), The Mollusca, Physiology. Academic Press, New York, pp. 467–504.

Waite, J.H., Vaccaro, E., Sun, C., Lucas, J.M., 2002. Elastomeric gradients: a hedge against stress concentration in marine holdfasts?. Philos. Trans. R. Soc. Lond. Ser. B: Biol. Sci. 357 (1418), 143–153.

Ward, P.D., 1980. Comparative shell shape distributions in jurassic-cretaceous ammonites and jurassic-tertiary nautilids. Paleobiology 6 (1), 32–43.

Ward, P., 1981. Shell sculpture as a defensive adaptation in ammonoids. Paleobiology 7 (1), 96–100.

Weitschat, W., 2008. Intraspecific variation of *Svalbardiceras spitzbergensis* (Frebold) from the early triassic (Spathian) of spitsbergen. Polar Res. 27 (3), 292–297.

Westermann, G.E., 1966. Covariation and taxonomy of the Jurassic ammonite *Sonninia adicra* (Waagen). N. Jahrb. Geol. Palaontol Abh. 124, 289–312.

Westermann, G., 1996. Ammonoid life and habitat. Ammonoid Paleobiol.

Westermann, B., Schmidtberg, H., Beuerlein, K., 2005. Functional morphology of the mantle of *Nautilus pompilius* (Mollusca, Cephalopoda). J. Morphol. 264 (3), 277–285.

[4] These calculations are explicitly given in the second paper in this series: Lessinnes, T., Moulton, D.E., Goriely, A., Morphoelastic rods: Part II: Growing birods, submitted.